Planar Plasmonic Focusing and Optical Transport Using CdS Nanoribbon

Zheyu Fang,[†] Chenfang Lin,[†] Renmin Ma,[†] Shan Huang,[†] and Xing Zhu[†,‡,*]

[†]School of Physics, State Key Laboratory for Mesoscopic Physics, Peking University, Beijing 100871, People's Republic of China, and [‡]National Center for Nanoscience and Technology, Beijing 100190, People's Republic of China

ABSTRACT Planar plasmonic focusing of surface plasmon polaritons (SPPs) by an in-plane nanostructure consisting of Ag-column arrays and an in-plane Fresnel zone plate (FZP) with a Cu grating underneath for energy compensation was demonstrated. The CdS-based hybrid plasmonic waveguide generated in the Ag-column arrays was characterized with a scanning near-field optical microscope. By using the FZP focusing structure, the SPP modes were separated from the CdS photoluminescence background and focused at the FZP focus area, and in this way, were used as the source for the SPP waveguide. Finite-difference time-domain simulations correspond with the experimental observations, suggesting that this is indeed an effective approach to control SPP coupling within the dielectric nanoribbon waveguide.

KEYWORDS: surface plasmon polariton · CdS nanoribbon · Fresnel zone plate · near-field optical microscopy · photoluminescence

Surface plasmon polaritons (SPPs) are collective electromagnetic excitations that propagate at an interface between dielectric and metal layers, evanescently confined perpendicular to the interface.[1] The polaritons are considered to be a potential optical data storage unit in highly integrated photonic devices owing to their high confinement near the interface and their intrinsic localization. Surface plasmonic crystals,[2,3] surface-enhanced Raman scattering,[4,5] surface-enhanced second harmonic generation,[6,7] *etc*. have been demonstrated as potential roles for SPP devices in resonance sensing and imaging applications. Progress in nanoscale fabrication has given rise to more fascinating applications in superimaging negative refraction metamaterial,[8−10] plasmonic lithography,[11,12] and plasmonic trapping,[13−15] as well as the biological sensing for cancer treatment[16] that have remarkably extended the horizons of plasmon research and development.

SPPs have been focused by coupling the light into SPP modes with an array of concentric circular metallic slits,[17] a planar circular grating milled into a Ag film,[18] or *V*-shaped channels etched in metal film with tapered ends.[19] However, all these focusing techniques are based on fabricated nanostructures, that is, SPP modes propagate along the track predefined by the structure and generate a huge field enhancement at the tapered end. This kind of SPP focusing induces a field disturbance caused by the predefined nanostructures, thus it cannot be used to investigate the origin of the SPP device's properties.

The real part of the SPP propagation constant $\beta = (2\pi/\lambda)[\varepsilon_d\varepsilon_m/(\varepsilon_d + \varepsilon_m)]^{1/2}$ is related to the SPP effective refractive index, $N_{eff} = (\lambda/2\pi)Re(\beta)$, where λ is incident laser wavelength, implying that a dielectric layer on a metal surface can result in a higher SPP index than a simple metal/air interface can have. The SPP subwavelength waveguide was proposed to overcome the diffraction limitation so as to realize the electromagnetic field confinement.[20−22] Hybrids of conventional dielectric waveguides exhibit the merits of both the dielectric photoluminescence (PL) guiding and the field enhanced SPP propagation.[23,24] However, controlling SPP coupling and extracting/separating SPP modes from the dielectric PL background are still challenges for further plasmonic applications in nanophotonic devices.

In this letter we report planar plasmonic focusing of SPPs by an in-plane nanostructure consisting of Ag-column arrays and an in-plane Fresnel zone plate (FZP) with a Cu grating underneath for energy compensation. A CdS-based hybrid plasmonic waveguide was formed in the Ag-column arrays. Using this planar SPP focusing process, the extraction/separation of SPP modes from the CdS PL background was realized and a focused SPP source at the FZP focus area was generated.

*Address correspondence to zhuxing@pku.edu.cn.

Received for review July 3, 2009 and accepted December 08, 2009.

Published online December 15, 2009.
10.1021/nn900729n

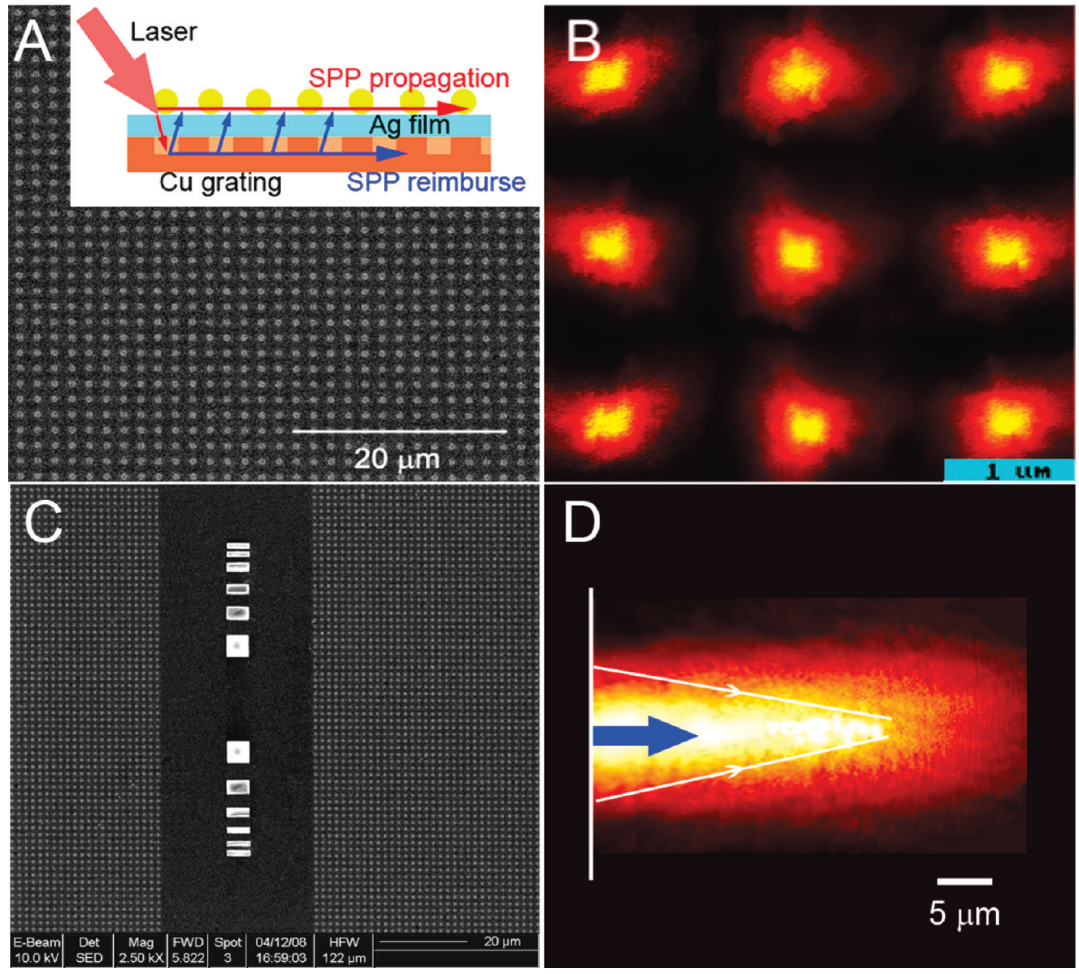

Figure 1. (A) SEM image of Ag-column arrays and schematic of Cu grating for SPP energy compensation (inset); (B) near-field optical image of SPP scattering during propagation in Ag-column arrays; (C) SEM image of Ag nanostructures with a 12-zone FZP for SPP focusing; (D) near-field optical image of SPP focusing with a 1 μm diameter focus spot.

RESULTS AND DISCUSSION

Our planar plasmonic focusing nanostructure is shown in Figure 1. Ag-column arrays and the in-plane Fresnel zone plate (FZP) structure with a Cu grating layer were fabricated by an electron beam lithography (EBL) and lift-off technique on the smooth Ag surface. Then, the CdS nanoribbon was moved into the target position by using a poly(methyl methacrylate)-mediated nanotransfer printing technique[25] (see Supporting Information Figure S1).

The SPP field enhancement and wave propagation with energy compensation were realized by using a subwavelength nanostructure fabricated on the Ag surface with a Cu grating underneath. The dispersion of SPP propagation at the interface between metal/dielectric layers is

$$k_{sp} = \omega/c(\varepsilon_M\varepsilon_d/(\varepsilon_M + \varepsilon_d))^{0.5} \quad (1)$$

where ε_M and ε_d are the real parts of the Ag and dielectric permittivities, respectively. With a *p*-polarized laser illuminating the Ag film, the surface electrical field can be enhanced by the SPP resonance when the phase-matching condition is fulfilled. The mismatch in wavevector between the in-plane momentum of impinging photons and k_{sp} can be compensated by using the Ag-column arrays (300 nm in diameter and 50 nm in height for our experiment) with an interval of 1.5 μm, as shown in Figure 1A.

The reverse process, SPP modes radiation can also take pace when the modes interact with the grating structure and satisfy the following condition,

$$k_{sp} = \omega/c \sin\theta \pm vg \quad (2)$$

where θ is the incident angle, *g* is the reciprocal vector of the grating, and *v* is an integer. In our experiment, a Cu grating, functioning as a reflection layer, was fabricated under the Ag nanostructure to restore the SPP energy lost during propagation (inset of Figure 1A). A large portion of the incident laser beam penetrates the Ag film (200 nm thick) and is scattered to the substrate rather than coupled to the SPP modes at the top surface. Thus the Cu grating underneath was used as a mirror to collect the laser transmissions and couple them back to the SPP modes. According to eq 2, these coupled SPP modes propagate and interact with the Cu grating at the incident wavevector, which, like an en-

ergy pump, was used to restore the top layer SPP energy losses during wave propagation. SPP radiation was imaged by scanning near-field optical microscopy (SNOM) when the SPP wave struck the Ag-column arrays from the left. Figure 1B is the near-field optical image of the surface nanostructures when the SPP wave is generated. The SPP energy dissipates from the radiation; however, because of the compensation from the Cu layer, a 82% propagation energy is reserved.

To show the advantage of our nanocolumn arrays (with Cu grating underneath) for coupling the SPP modes, three other kinds of structures (nanohole arrays, nanogrooves, and nanocolumn arrays with no Cu grating underneath) have been compared for scattering radiation loss. The SPP energy is considered from the reflectivity (R), in-plane transmission (T), and SPP extinction (E). And the losses (SPP extinction) can be obtained from the relationship

$$T + R + E = 1 \tag{3}$$

where the SPP extinction (E) accounts for both scattering radiative losses and intrinsic damping of SPP traveling along the metal film. The SNOM optical fiber (coated with Al) was used to scan the sample surface, providing the mapping of the SPP electric field intensity. The near-field images were taken by keeping the fiber tip at a constant distance, about 150 nm from the sample surface. However, the radiative contribution was too strong in the nanostructure area and the SNOM signal recorded at these points was no longer proportional to the evanescent field intensity of either the incident or the output SPP. Thus, the equation $T = I_{out}/I_{in}$ has to be adapted to account for the intrinsic damping with propagation distance of the surface plasmon as[27]

$$T = \left(\frac{I_{out}}{I_{in}}\right) e^{(d_{in}+d_{out})/L_{sp}} \tag{4}$$

where L_{sp} represents the SPP propagation length (damping distance), and d_{out}, d_{in} denote the distance between the detection place and the incident spot. The propagation length, L_{sp}, defined as the distance for which the SPP field intensity decays to 1/e of its value, is $L_{sp} \approx 24$ μm, calculated using the dielectric constant of Ag from ref 26. Since L_{sp} depends strongly on the thickness of the metal film, its quality, and its actual dielectric constant, we have determined its value experimentally for our nanostructures. The SPP propagation length is obtained by fitting the intensity to the formula,

$$I = I_0 e^{(-x/L_{sp})} \tag{5}$$

And we find a propagation length value of $L_{sp} = 23.2 \pm 0.2$ μm, which is in good agreement with the expected value for the Ag film, $L_{sp} \approx 24$ μm. The difference is probably related to the Ag film's roughness (rms = 2 nm) and possible variations in dielectric constant between our evaporated Ag films and the data collected by Palik.[26] Then, the propagation $T = 82\% \pm 15\%$ is obtained. (The uncertainty includes the deviation in the measure of L_{sp}, the error in the determination of the distances of d_{in} and d_{out}, and the dispersion in the average.) The reflection (R), calculated in a similar way, is $R = 14\% \pm 3\%$, and finally the SPP extinction (E) in this structure can be safely concluded to be less than 10%. Using the same method, the SPP extinction in nanohole arrays, nanogrooves, and nanocolumn arrays with no Cu grating underneath are estimated as 60%, 70%, and 30%, respectively (see Supporting Information Text S2). Finally, we can conclude that the nanocolumn array with Cu grating underneath is the best of these structures for SPP coupling and propagation.

The in-plane Fresnel zone plate, consisting of a series of zones alternating in transmittance between transparent and opaque, was used to focus the SPP waves, as shown in Figure 1C. Considering the diffraction of the SPP wave striking this structure from the left, the constructive interference of the SPP fields can be obtained at a focal distance f when the Fresnel zone radii r_n satisfy

$$r_n = \sqrt{n\lambda_{spp} f + \frac{n^2 \lambda_{spp}^2}{4}} \tag{6}$$

where n is an integer and λ_{spp} is the SPP wavelength. For a planar FZP, r_n are boundary positions where transmittance changes between transparent and opaque. A 12-zone FZP with radii given by eq 6 was constructed at an Ag/air interface with a focal length $f = 60$ μm. By using the Ag-column arrays integrated on both sides, the SPP wave propagation and focusing were both revealed by the structure radiations detected by SNOM. Figure 1d is the near-field optical image of SPPs, focusing where the focus spot is about 1 μm diameter. Taking into account the effective detection point located at about 100 nm above the FZP focus, we obtained about 15 times as an average estimate of the field intensity enhancement at the focal length of 60 μm. The nonpattern SPP focusing improves the contrast and longitudinal resolution of the SPP imaging, and does not initiate the field disturbance from the structures like circular grating or metallic slits, *etc*. as mentioned before.[17,18] If the focusing SPPs can be effectively coupled into the CdS nanoribbon, the separation of SPP *in situ* excitation and guided wave detection can be realized, which solves the problem of SPP modes being mixed with the CdS PL background and can be used to generate a novel SPP waveguide.

The CdS nanoribbon used in the experiment was synthesized by physical evaporation in the presence of the Au film catalyst (see Supporting Information Figure S3). Figure 2 is the TEM image of a single CdS nanoribbon and its electron diffraction picture (inset). These nanoribbons possess fairly uniform rectangular cross

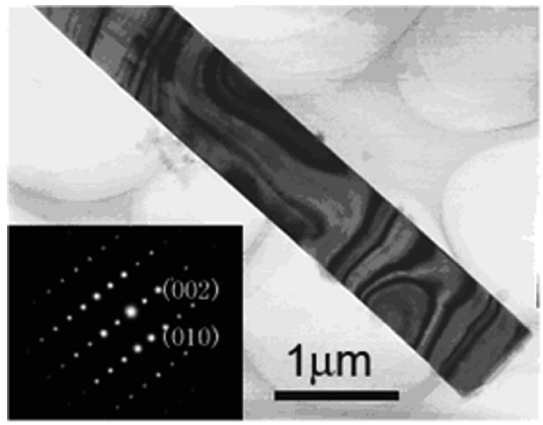

Figure 2. TEM and electron diffraction (inset) image of CdS nanoribbon.

sections around 1.0 μm × 300 nm. Their PL spectra were detected by SNOM in the Ag-column arrays and FZP focus area, respectively.

The spatially resolved PL spectra of the CdS nanoribbons deposited in the Ag-column arrays perpendicular and parallel to the SPP wavevector were compared, as shown in Figure 3A,B. Both nanoribbons have the same geometry and chemical properties. The incident laser beam (442 nm) with a 2 μm diameter illuminated the sample in *p*-polarization. The SNOM fiber probe was paused at the ribbon end to detect the near-field emission spectra; meanwhile the laser focus was moved along the ribbon to alter the waveguide length. For the case of nanoribbons normal to the SPP wavevector, because the SPP resonance was confined at the laser focus area, only the CdS PL wave was formed in the waveguide and detected at the end facet of the ribbon by the SNOM tip. The emission spectra from waveguides of different lengths were recorded and compared in Figure 3C. The photon energy 2.35 eV is the CdS absorption peak and its intensity decreases when the propagation distance changes from 1 to 30 μm. The 46 meV red-shift of the energy peak is induced by the semiconductor self-absorption effect; that is, Urbach tail, an extension of the density of state into the band gap near the main edges of the bands, give rise to an exponential tail near the fundamental absorption edge at the long wavelength direction.[28,29]

Figure 3D shows the near-field PL spectra of the nanoribbon perpendicular to the SPP wavevector. Besides the CdS absorption peak 2.35 eV, other energies are also recorded in the spectra and cannot be distinguished. The excitation for SPP guided modes is given by the phase matching condition,

$$k_0 n_1 \sin\theta \sin\delta = k_0 R(n_{\text{eff}}) \qquad (7)$$

where k_0 is the free space wavevector, n_1 is the refractive index of dielectric, n_{eff} is the associated complex effective index ($n_{\text{eff}} = \nu + \iota\alpha$). Only the real part of n_{eff} is used in eq 7 since the Ag layer is a source of Ohmic and radiative losses. With the incident wavevector, the excited SPPs can be effectively coupled with the nanoribbon and confined at the interface between the CdS and Ag layers. With the waveguide length increasing, the emission intensity decreases and the CdS absorption peak shifts, which can be explained by the same reason (Urbach tail) as described for Figure 3C. On the other hand, we thought that the energy mixture seen in

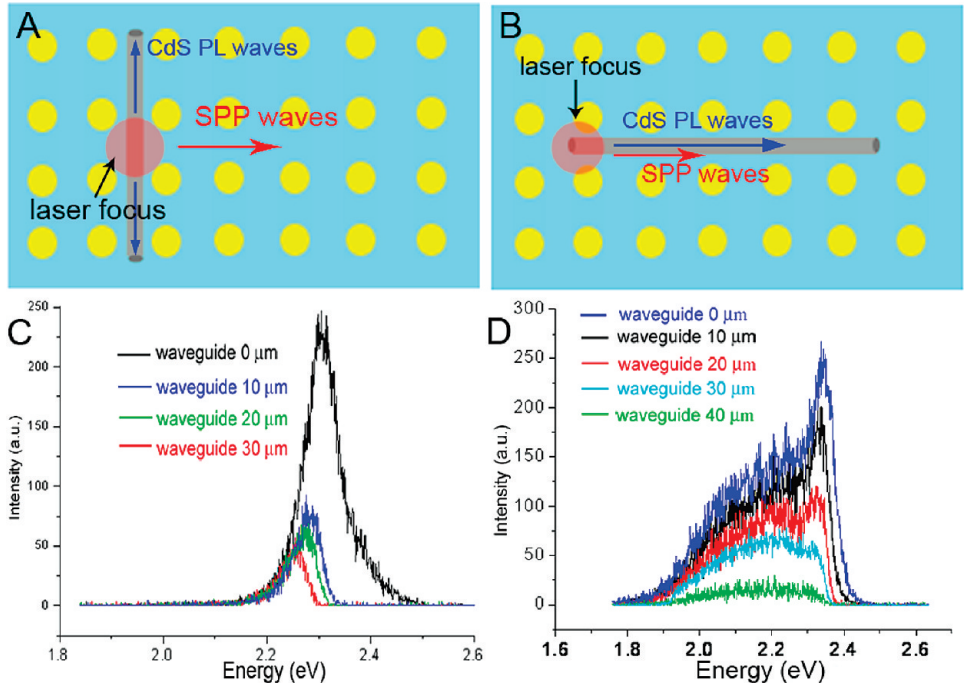

Figure 3. (A and B) Schematic images of CdS nanoribbons deposited perpendicular (A) and parallel (B) to the SPP wavevector in the Ag-column arrays; (C and D) near-field optical spectra recorded by SNOM at the emission end of nanoribbons in panels A and B, respectively.

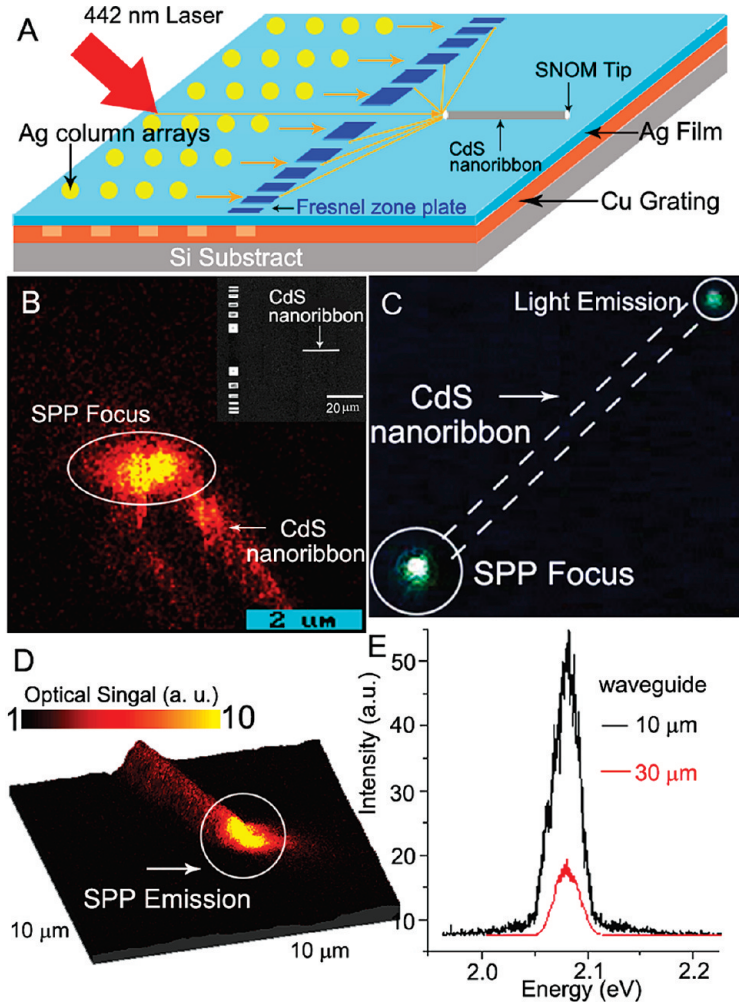

Figure 4. (A) Sketch of focused SPP coupled into CdS nanoribbon; (B) near-field optical image of SPP scattering with the ribbon end at the FZP focus. Inset is a schematic of nanoribbon deposited perpendicular to the SPP wavevector with one end close to the FZP focus area; (C) SPP scattering at the FZP focus and emission at the other end of the ribbon captured by a color CCD in far-field; (D) three-dimensional near-field optical plot of SPP emission from nanoribbon's end; (E) near-field optical spectra of SPP emission for different waveguide lengths recorded by SNOM.

the spectra might be induced by the energy coupling between the Ag columns' SPP modes and CdS's PL modes. To verify this, the polarization of the incident laser was switched from *p* to *s* mode, that is, no SPP resonance. Without SPP resonance, the corresponding spectra were almost the same as the curves in Figure 3C, which proves that a hybrid plasmonic waveguide based on the CdS nanoribbon has been successfully generated.

To extract the SPP signal from the CdS PL background and generate a novel SPP waveguide, a single nanoribbon (parallel to the SPP wavevector) was deposited at the FZP focus area (Figure 4A). The SPP focusing concentrated the electrical fields into a 1 μm sized spot, as shown in Figure 1D. In our configuration, the in-plane (rather than perpendicular) method was used to stimulate this CdS waveguide. And the excitation source was the focused plasmons, that is, no CdS PL modes would be excited. (The dielectric PL light was used as the excitation source in Dalton's configuration.[3]) However, in many previous SPP investigations, plasmon modes and light modes were always mixed together since the SPP excitation and detection processes took place in the same structure or configuration. In our case, the SPP excitation and detection structures are located in different places (the left and right side of the FZP structure). Thus, the SPP modes can be successfully extracted/separated from the PL background.

Because the metallic nanowires (Ag, Au) always suffer huge Ohmic losses, the SPP propagation length based on metallic nanowires is limited to 10 μm at visible wavelengths, which has also been demonstrated by Dalton's group (9.1 μm).[3] Using the dielectric waveguide on the metal surface results in a higher refractive index for a SPP wave on the metal−dielectric interface compared to a metal−air interface, giving rise to SPP modes bound by the dielectric ribbon similar to the guided modes in conventional optical fibers. Thus CdS-loaded SPP waveguides were used for low edge-scattering losses in comparison to the bare Ag nanowire waveguides.[3]

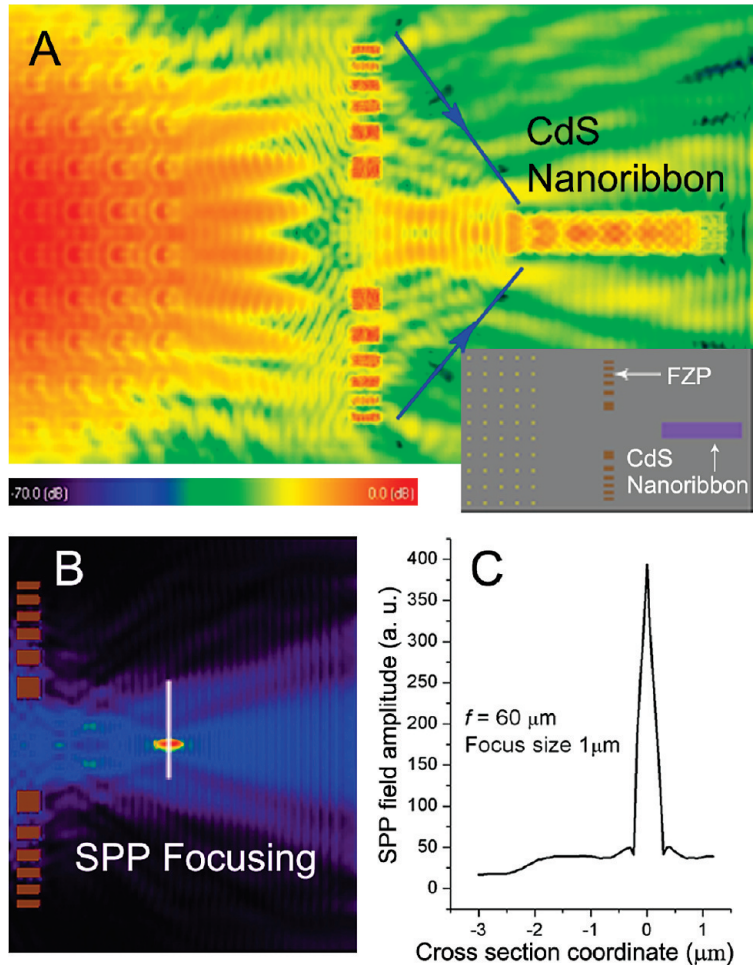

Figure 5. (A) FDTD simulation of SPP propagation, focusing, and coupling (see inset for FDTD schematic); (B) electrical field distribution for SPP focusing at 60 μm focal length with 1 μm diameter spot; (C) maximum field enhancement calculated at the FZP focus is about 200.

The SPP scattering at the incident end facet and the leakage radiation from the ribbon edges were detected by SNOM, indicating that the guided SPPs are extremely confined by the CdS nanoribbon, as shown in Figure 4B. Inset is a schematic of the nanoribbon deposited lateral to the SPP wavevector with one end close to the FZP focus area. Thus, separation of SPP modes from the CdS PL background was realized, and a novel SPP waveguide based on CdS nanoribbons was obtained.

The SPP emission light was also imaged by both the color CCD in the far-field and the SNOM in the near-field (Figure 4C,D). The 3-dimensional near-field plot shows good SPP confinement and strong end radiation. A single energy peak was recorded by SNOM, and there was no shift when the waveguide length was increased from 10 to 30 μm (Figure 4E). Because of the nonpatterned reality of this kind of SPP focusing, only the electrical field intensity is concentrated at the FZP focused area, and the SPP frequency remains unchanged. Thus the spectra detected from the nanoribbons' emission should have the same SPP frequency with the one induced by the Ag-column arrays. This has been verified by the calculation of eq 1 and 2; a good agreement with the recorded plasmon energy of 2.09 eV in the near-field is obtained.

The CdS nanoribbon with a cross-section of 1.0 × 0.3 μm was illuminated by the SPP focused spot with a diameter of 1.0 μm. Since the penetration depth of the SPP in air is about 0.34 μm, the efficiency of coupling (C_1) between the focused plasmon modes and the nanoribbon's incident facet can be estimated to be 88%. The final coupling efficiency (C_2) between the focused plasmon modes and the emission nanoribbon modes is estimated by calculating the ratio between the intensity at the emission end of the nanoribbon and the intensity at the FZP focus (with no nanoribbon) in the near field. We find that C_2 is about 76% for a 10 μm CdS nanoribbon, but it decreases to 26% when the nanoribbon length increases to 30 μm. The difference between C_1 and C_2 contributes to SPP scattering at the incident facet and to energy losses induced by SPP propagation along the nanoribbon. Because the nanocolumn structure with a Cu grating underneath has been proven to obtain a 82% propagation energy, the overall coupling efficiency (C_3) from the incident laser

beam to the nanoribbon (10 μm) emission modes can be 62.3% (76% × 82%).

To gain further insight into this CdS-based plasmonic waveguide, the SPP focusing and SPP coupling with the nanoribbon were simulated by finite-difference time-domain (FDTD) calculations using an eigenmode solver at the front edge boundary. The simulation results support the conclusion that the FZP structure plays a role in focusing the SPP waves from the left (Figure 5A), and they correspond with the experimental observations, which found the strongest enhancement at the FZP focus area. The occurrence of a bright spot in near-field optical images (Figure 4B,C) and the interference fringes indicating the focused SPPs are effectively coupled into the nanoribbon. The best coupling efficiency (with respect to the field enhancement achieved at the FZP focus) for a given focal length was found for the width of 1 μm, as expected (the same as the focus size), with the optimum focal length $f = 60$ μm, and the direction parallel to the SPP wavevector (Figure 5B). The field enhancement as estimated from the calculations is about 200 times for a focal length 60 μm and a 1 μm diameter spot (Figure 5C). The discrepancy with the experimental results should be expected given the surface roughness induced by the electron beam evaporation and the fact that the maximum field intensity was calculated to be fairly close to the FZP focus.

CONCLUSIONS

We have demonstrated our planar plasmonic focusing nanostructure, which plays the role of SPP excitation, propagation, and focusing by using Ag-column arrays and in-plane FZP structures with a Cu grating underneath. When the incident laser directly illuminates the CdS nanoribbon, the resonant SPP modes are mixed with the CdS PL waves during the propagation, as indicated in the near-field spectra. In contrast, by using this planar plasmonic focusing, we have successfully used focused SPP modes to investigate plasmonic waveguides based on CdS nanoribbons to extract/separate the SPP signal from the CdS PL background when the nanoribbon is parallel to the incident SPP wavevector. The near-field spectra measured at the emission end of CdS nanoribbons detect only the SPP energy 2.09 eV, which corresponds with the theoretical calculation and the FDTD simulation of SPP focusing and coupling. Our result demonstrates a novel approach for planar plasmonic focusing and the extraction of SPP modes from dielectric PL background. This may have potential applications for plasmonic devices, especially for integrated optoelectronic waveguides.

METHODS

Fabrication of Ag-Column Arrays and FZP Structure. (i) A 1.5 μm thick polymethyl methacrylate (PMMA) was spun-coated onto a cleaned Si plate, and 5 μm wide FZP features were defined in PMMA by EBL patterning; (ii) a 400 nm thick film of Al was deposited over the PMMA mask, and then using an acetone lift-off procedure the Al masks were generated; (iii) the Si substrate was etched 2 μm deep except behind the Al masks, thus the Si-based in-plane FZP was fabricated; (iv) after the Cu grating layer (150 nm thick, deposited by electron beam evaporation) was fabricated by focused ion beam (FIB) etching, a 200 nm thick Ag film was deposited by evaporation and the column arrays were fabricated on the top surface by using EBL and a lift-off technique.

Scanning Near-field Optical Microscopy. SNOM spectroscopy consists of a scanner NSOM-100 (Nanonics Co.), an electronic controller SPM-1000 (RHK Co.) and a spectrometer iHR550 (Jobin Yvon Co.). The scanner was situated on the sample stage of an optical microscope (Olympus IX70). The near-field tip used in this experiment was an Al-coated, tapered cantilever optical fiber with a 100 nm apex diameter (Nanonics Co.). A He−Cd laser illuminated the Ag structures in *p*-polarization. SNOM with a resolution higher than the diffraction limit is a crucial technique to detect the SPP resonance enhancement and can be used to record the near-field PL spectra at any part of the sample surface; hence it provides more detailed insight than the signal received in far-field, that is, conventional optical microscopy (for the setup, see Supporting Information Figure S4).

Theoretical Methods. FDTD was used to calculate the electromagnetic field distribution at the interface between the metal and dielectric layers as well as at the inside and outside of the nanoribbons, so as to provide the complex effective index of the guided mode. The Ag columns (300 nm diameter and 50 nm height) with a 12-zone FZP structure were modeled on a Ag film (200 nm thick, permittivity = −7.6321 + 0.7306i), which is the same as the experimental structure. The arrays were separated with an interval of 1.5 μm and illuminated by a *p*-polarized Gaussian beam ($\lambda = 442$ nm). The CdS nanoribbons (refractive index 2.64) with width from 0.5 to 1.5 μm were modeled to support the SPP coupling with an end placed close to the FZP focus perpendicular or parallel to the SPP wavevector. The simulations were calculated by the commercial software XFDTD (Remcom, Inc.). For the movie of the simulation of SPP propagation, focusing, and coupling to CdS nanoribbon, see Supporting Information.

Acknowledgment. This work is supported by the National Natural Science Foundation of China (Grant No. 10574002) and the National Basic Research Program of China (973 Program) Grant No. 2007CB936800.

Supporting Information Available: Figure S1 illustrates of the procedures of PMMA-mediated transfer printing technique; text S2 details of the advantages of nanocolumn arrays for coupling SPP; Figure S3 details CdS nanoribbons; Figure S4 is a schematic of SNOM and experimental process; a movie shows the simulation of SPP propagation, focusing, and coupling. This material is available free of charge *via* the Internet at http://pubs.acs.org.

REFERENCES AND NOTES

1. Barnes, W. L.; Dereux, A.; Ebbesen, T. W. Surface Plasmon Subwavelength Optics. *Nature* **2003**, *424*, 824–830.
2. Volkov, V. S.; Bozhevolnyi, S. I.; Leosson, K.; Boltasseva, A. Experimental Studies of Surface Plasmon Polariton Band Gap Effect. *J. Microsc.* **2003**, *210*, 324–329.
3. Pyayt, A.; Wiley, B.; Xia, Y. N.; Chen, A. T.; Dalton, L. Integration of Photonic and Silver Nanowire Plasmonic Waveguides. *Nat. Nanotechnol.* **2008**, *3*, 660–665.
4. Kneipp, K.; Wang, Y.; Kneipp, H.; Perelman, L. T.; Itzkan, I.; Dasari, R. R.; Feld, M. S. Single Molecule Detection Using Surface-Enhanced Raman Scattering (SERS). *Phys. Rev. Lett.* **1997**, *78*, 1667–1670.
5. Nie, S. M.; Emory, S. R. Probing Single Molecules and Single Nanoparticles by Surface-Enhanced Raman Scattering. *Science* **1997**, *275*, 1102–1106.

6. Chen, C. K.; de Castro, A. R. B.; Shen, Y. R. Surface-Enhanced Second-Harmonic Generation. *Phys. Rev. Lett.* **1981**, *46*, 145–148.
7. Kim, E. M.; Elovikov, S. S.; Murzina, T. V.; Nikulin, A. A.; Aktsipetrov, O. A.; Bader, M. A.; Marowsky, G. Surface-Enhanced Optical Third-Harmonic Generation in Ag Island Films. *Phys. Rev. Lett.* **2005**, *95*, 227402/1–227402/4.
8. Smolyaninov, I. I.; Elliott, J.; Zayats, A. V.; Davis, C. C. Far-Field Optical Microscopy with a Nanometer-Scale Resolution Based on the In-Plane Image Magnification by Surface Plasmon Polaritons. *Phys. Rev. Lett.* **2005**, *94*, 057401/1–057401/4.
9. Smolyaninov, I. I.; Hung, Y. J.; Davis, C. C. Magnifying Superlens in the Visible Frequency Range. *Science* **2007**, *315*, 1699–1701.
10. Zhang, X.; Liu, Z. W. Superlenses to Overcome the Diffraction Limit. *Nat. Mater.* **2008**, *7*, 435–441.
11. Liu, Z. W.; Wei, Q. H.; Zhang, X. Surface Plasmon Interference Nanolithography. *Nano Lett.* **2005**, *5*, 957–961.
12. Srituravanich, W.; Fang, N.; Sun, C.; Luo, Q.; Zhang, X. Plasmonic Nanolithography. *Nano Lett.* **2004**, *4*, 1085–1088.
13. Righini, M.; Zelenina, A.; Girard, C.; Quidant, R. Parallel and Selective Trapping in a Patterned Plasmonic Landscape. *Nat. Phys.* **2007**, *3*, 477–480.
14. Righini, M.; Volpe, G.; Girard, C.; Petrov, D.; Quidant, R. Surface Plasmon Optical Tweezers: Tunable Optical Manipulation in the Femtonewton Range. *Phys. Rev. Lett.* **2008**, *100*, 186804/1–186804/4.
15. Fang, Z. Y.; Lin, F.; Huang, S.; Song, W. T.; Zhu, X. Focusing Surface Plasmon Polariton Trapping of Colloidal Particles. *Appl. Phys. Lett.* **2009**, *94*, 063306/1–063306/3.
16. Loo, C.; Lowery, A.; Halas, N.; West, J.; Drezek, R. Immunotargeted Nanoshells for Integrated Cancer Imaging and Therapy. *Nano Lett.* **2005**, *5*, 709–711.
17. Verhagen, E.; Polman, A.; Kuipers, L. Nanofocusing in Laterally Tapered Plasmonic Waveguides. *Opt. Exp.* **2008**, *16*, 45–57.
18. Steele, J. M.; Liu, Z. W.; Wang, Y.; Zhang, X. Resonant and Non-resonant Generation and Focusing of Surface Plasmons with Circular Gratings. *Opt. Exp.* **2004**, *14*, 5664–5670.
19. Volkov, V. S.; Bozhevolnyi, S. I.; Rodrigo, S. G.; Martin-Moreno, L.; Garcia-vidal, F. J.; Devaux, E.; Ebbesen, T. W. Nanofocusing with Channel Plasmon Polaritons. *Nano Lett.* **2009**, *9*, 1278–1282.
20. Bozhevolnyi, S. I.; Volkov, V. S.; Devaux, E.; Laluet, J.-Y.; Ebbesen, T. W. Channel Plasmon Subwavelength Waveguide Components Including Interferometers and Ring Resonators. *Nature* **2006**, *440*, 508–511.
21. Ozbay, E. Plasmonics: Merging Photonics and Electronics at Nanoscale Dimensions. *Science* **2006**, *311*, 189–193.
22. Fang, Z. Y.; Zhang, X. J.; Liu, D.; Zhu, X. Excitation of Dielectric-Loaded Surface Plasmon Polariton Observed by Using Near-Field Optical Microscopy. *Appl. Phys. Lett.* **2008**, *93*, 073306/1–073306/3.
23. Oulton, R. F.; Sorger, V. J.; Genov, D. A.; Pile, D. F. P.; Zhang, X. A Hybrid Plasmonic Waveguide for Subwavelength Confinement and Long-Range Propagation. *Nat. Photonics* **2008**, *2*, 496–500.
24. Fang, Z. Y.; Huang, S.; Lin, F.; Zhu, X. Color-Tuning and Switching Optical Transport through CdS Hybrid Plasmonic Waveguide. *Opt. Exp.* **2009**, *17*, 20327–20332.
25. Jiao, L. Y.; Fan, B.; Xian, X. J.; Wu, Z. Y.; Zhang, J.; Liu, Z. F. Creation of Nanostructures with Poly(methyl methacrylate)-Mediated Nanotransfer Printing. *J. Am. Chem. Soc.* **2008**, *130*, 12612–12613.
26. Palik, E. D. *Handbook of Optical Constants of Solids*; Academic: San Diego, 1985.
27. Gonzalez, M. U.; Weeber, J. C.; Baudrion, A. L.; Dereux, A.; Stepanov, A. L.; Krenn, J. R.; Devaux, E.; Ebbesen, T. W. Design, Near-Field Characterization, and Modeling of 45° Surface-Plasmon Bragg Mirrors. *Phys. Rev. B* **2006**, *73*, 155416/1–155416/13.
28. Pan, A. L.; Liu, D.; Liu, R. B.; Wang, F. F.; Zhu, X.; Zou, B. S. Optical Waveguide through CdS Nanoribbons. *Small* **2005**, *1*, 980–983.
29. Pan, A. L.; Wang, X.; He, P. B.; Zhang, Q. L.; Wang, Q.; Zacharias, M.; Zhu, X.; Zou, B. S. Color-Changeable Optical Transport through Se-Doped CdS 1D Nanostructures. *Nano Lett.* **2007**, *7*, 2970–2975.